VISTA Status Report
June 1996

R. Martins, H. Puchner, S. Selberherr, T. Simlinger, W. Tuppa.

Institute for Microelectronics
Technical University Vienna
Gusshausstrasse 27-29
A-1040 Vienna, Austria

Contents

1 VMAKE 2.0 – Project Orientation and Parallel Compilation

1.1 New Features

The new version of the Vienna Make utility (**VMake**) is characterized by a redesign of several core routines and essential data structures, which resulted in much higher performance and flexibility. The latter enabled the incorporation of new valuable features, most notably the project orientation and the support for parallel compilation and linking on a workstation cluster [1].

The project orientation allows the managment of many separate software projects, accounting for the inter-project dependences. This applies also to installed projects, i.e., when a newer version of a library (i.e., the library project) is installed **VMake** will re-link all dependent programs of a project in work. Thus, global version consistency is maintained across all projects under **VMake** control. On the other hand, one has to locally check out and compile only the project which is to be worked on. The inter-project dependence of each project is specified in a local `vmake.prj` file (see Fig. 1). This makes it possible to split up a large project (like `VISTA`) into smaller, easier-to-handle ones and, at the same time, facilitates the integration of new software.

The parallel compilation feature allows one to utilize a whole cluster of workstations to build whole software projects in a fraction of the usual time. Determination and representation of the dependence information have been so designed that inherent parallelisms can be detected and used to speed up the build process considerably.

1.2 Algorithm

make and imake–based approaches usually must perform multiple passes over a project source tree to reach a certain build goal, during which many possibly non–needed files are rebuilt. **VMake** exploits the fine–grained global dependency information (over directory and project boundaries) to rebuild an utmost concise superset of the really required files. Internally **VMake** identifies each file by a unique `LISP` object which stores all available information about that file. The main agent checks the dependencies between objects (and possibly rebuilds the dependencies from modified source files) in a "depth first" algorithm and sends a rebuild request to the checked objects if required. If execution of a goal is required, the appropriate command is inserted into the sub–agent of **VMake** for later execution which occurs in parallel on a defined workstation cluster. This speeds up the build process significantly (by a factor of four, using seven DEC Alpha workstations compared to local execution). In contrast to make **VMake** needs no recursive evocation and solves the goal evaluation in one pass since all information is available in the main agent. Due to this strategy, **VMake** is significantly more efficient than make whenever the source code involved is spread around several different directories and/or projects. This helps to save resources which is important for restrictive operating system configurations.

Dependencies are stored in **VMake** for directly included source files only (in contrast to make where all include files over all levels are needed as dependencies). This speeds up the dependency generation process since no files are multiply scanned during dependency generation and so allows dependency generation on the fly on every run of **VMake**. The automatically extracted global information about projects is saved by **VMake** for every configuration in a special place to be reloaded on the next invocation.

1.3 The Queuing Agent

This sub–agent of **VMake** is activated by objects if they need to be rebuilt. In this case the queuing agent checks if all required inputs of a goal are already available and then queues it for building, otherwise it delays this job until all required objects are built. Objects ready for building are produced in parallel on the defined hosts and/or batch queues for the actual configuration. The main agent can request information about the current status of the queuing agent.

1.4 Project Installation and Version Managment

In contrast standard tools like make usually copy all files every time and do not create an information file. One additional feature is that only modified files, especially include files, are installed if an older release already exists. So only changed sources get new time stamps and again only a minimal set of files has to be rebuilt in the working project. Files that are no longer required in an installation are automatically removed from the global directory. To allow easy update from the repository **VMake** is able to update on project basis from the repository. The developer is informed of updated files and a warning is issued for every conflict between local modifications and the repository state.

```
;;- project definition file for the Sketch tool

(Project-Definition SketchTool
                    :fname "sketch"
                    :major      0
                    :minor      0
                    :patchlevel 0
                    :depend ViennaBaseSystem
                            Geometry2DSupport
                            AttributeSupport
                            PifApplicationInterface
                            PifToolBox
                            Materials
                            Layout
                    :manual "Sketch"
)
```

Figure 1: **VMake** project file: The `:depend` key lists all other projects on which this project depends.

2 Layout Data in VISTA

To close the gap between ECAD and TCAD it is required that VISTA can access lateral layout information. For this purpose converters from the most representative layout data formats to PIF were made available. Both the Caltech Interchange Format (CIF) and Calma's GDSII layout data formats are currently supported.

2.1 Integration within VISTA and User Interface

As the PIF Editor is used to specify device geometries it seemed logical that the converters were integrated in this tool. Layout data can be imported, modified if necessary, and be prepared for subsequent simulations. For that purpose a new menu item labeled **Layout** (see Figure 2) has been added to PED.

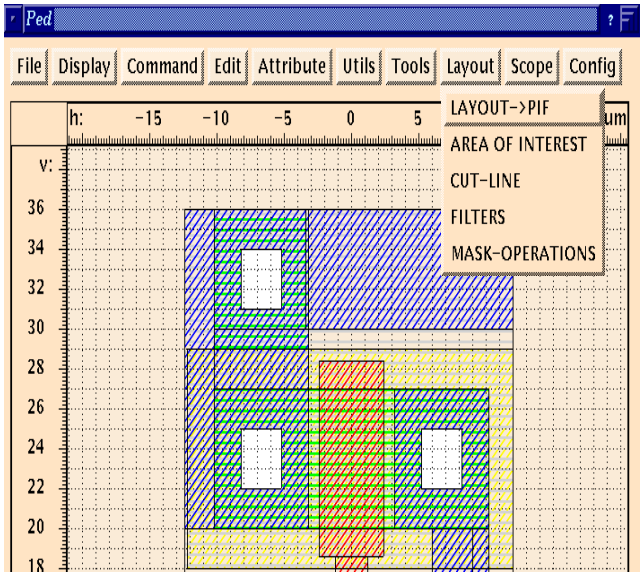

Figure 2: The **Layout** menu.

Besides the conversion to PIF, some basic layout handling features are also provided (see Figure 3). In an extension to the default geometric functions (i.e., drawing points, lines, faces, segments, and assigning materials, etc.) that already existed in PED, some new features for layout handling were added:

- Selection of areas of interest.
- Boolean operations with masks.
- Mask-name specified hide/show capabilities (filters).
- Cut-line specification.

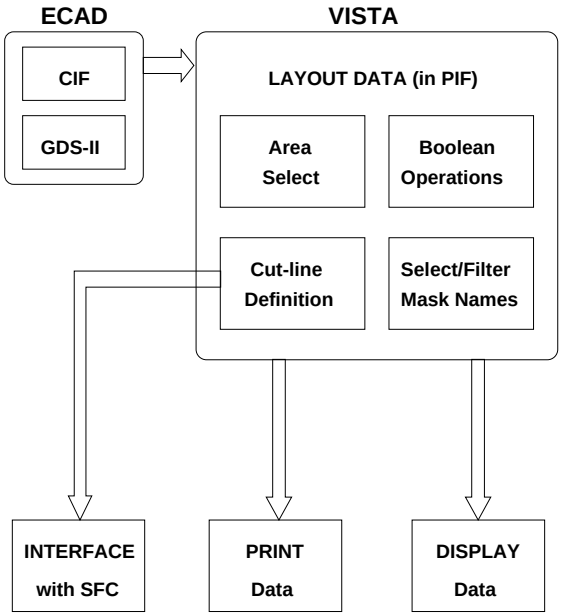

Figure 3: Layout data in Vista - Block diagram.

2.2 The specification of cut-lines

Since most process and device simulators integrated in VISTA are two-dimensional, there is the necessity to be able to specify cross-sections in terms of cut-lines in the circuit layout. These are the locations where a cut perpendicular to the layout plane will be performed. For three-dimensional simulations the area of interest takes the role of the cut-line to specify the simulation domain. This task is done in a user-friendly way and warnings about possible misuses, like the specification of a cut-line in a layout with large changes in the direction orthogonal to the cut-line, are automatically detected an reported. To better understand the concept, a simple example is presented in Figure 4. A more complex example is shown in Figure 5.

2.3 Interface with the SFC

The result of the cut-line tool is stored in a LISP like syntax format (see Figure 6) that is understood by the VISTA's Simulation Flow Control module (SFC), so the process simulations can be carried without the user explicitly defining the absolute edge coordinates. This allows to keep process and layout information separate in order not to clutter a process file with device specifics.

2.4 Examples

An example of how accurate interconnect wire capacitances can be extracted with VISTA using the Smart Capacitance Analysis Program (SCAP) is presented in Figure 7. Here the geometry to simulate is obtained by specifying a cut-line in a piece of layout imported from an ECAD framework.

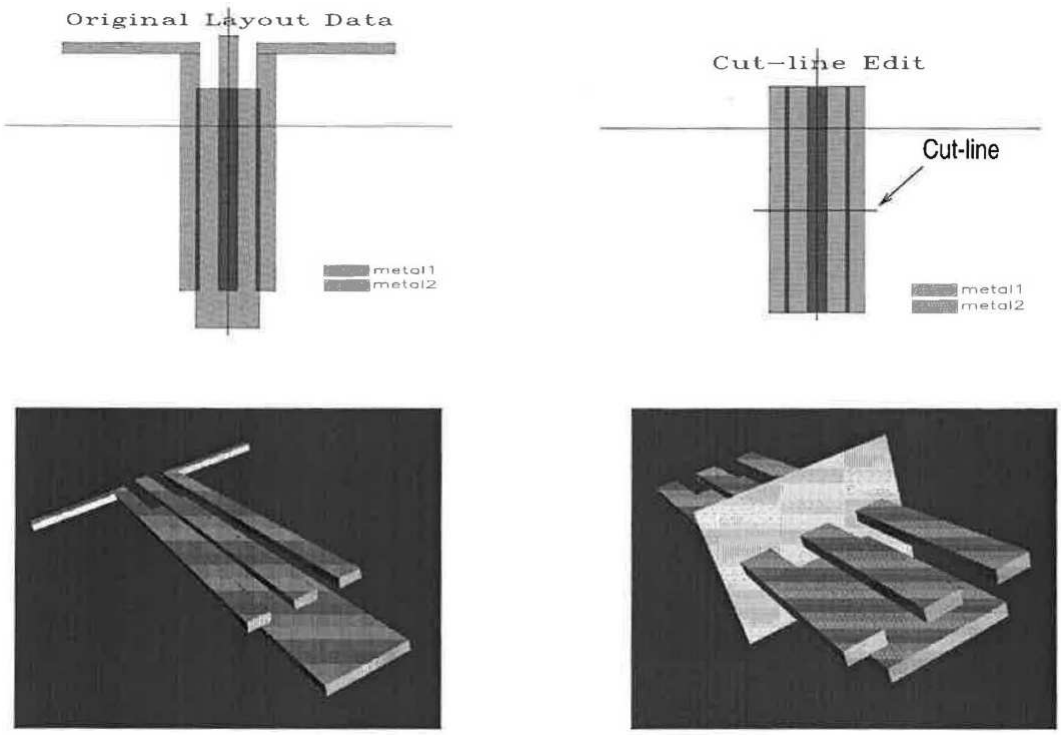

Figure 4: The cut-line concept.

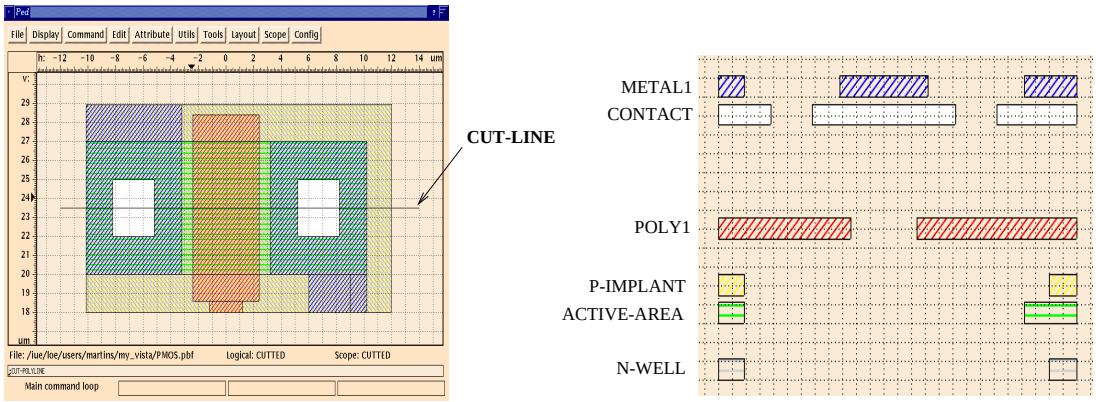

a) b)

Figure 5: A cut-line example: a) Layout with cut-line b) The mask openings at cut-line

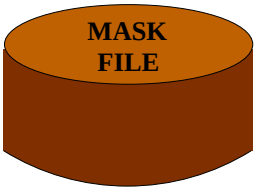

STRUCTURE:

```
;The MASK-FILE structure
(MASK_SET  <name>
   (LAYOUT  "layout_file")
   (UNITS  <unit>)
   (SCALE  <num> )
   (CUTLINE  <coord-pairs> )
   (MASK <mask_name>
      (DIMENSION  <1D | 2D>)
      (TRANSMITANCE  <value>)
      (PHASE <value>)
      (COORDS <list_of_coords>)
   )
   ⋮
)
```

EXAMPLE:

```
;The PMOS transistor MASK-FILE
(MASK_SET Low_power
   (LAYOUT PMOS.cif)
   (UNITS um)
   (SCALE 1)
   (CUTLINE  -12.00000   +23.50000
             +14.03330   +23.50000)
   (MASK POLY1
      (DIMENSION 1D)
      (TRANSMITANCE 0)
      (PHASE 0)
      (COORDS  9.60000   14.40000
               +26.03330)
   )
   (MASK ACTIVE-AREA
      (DIMENSION 1D)
      (TRANSMITANCE 0)
      (PHASE 0)
      (COORDS 1.85000   22.20000
               +26.03330)
   )
   ⋮
)
```

Figure 6: The mask-file syntax.

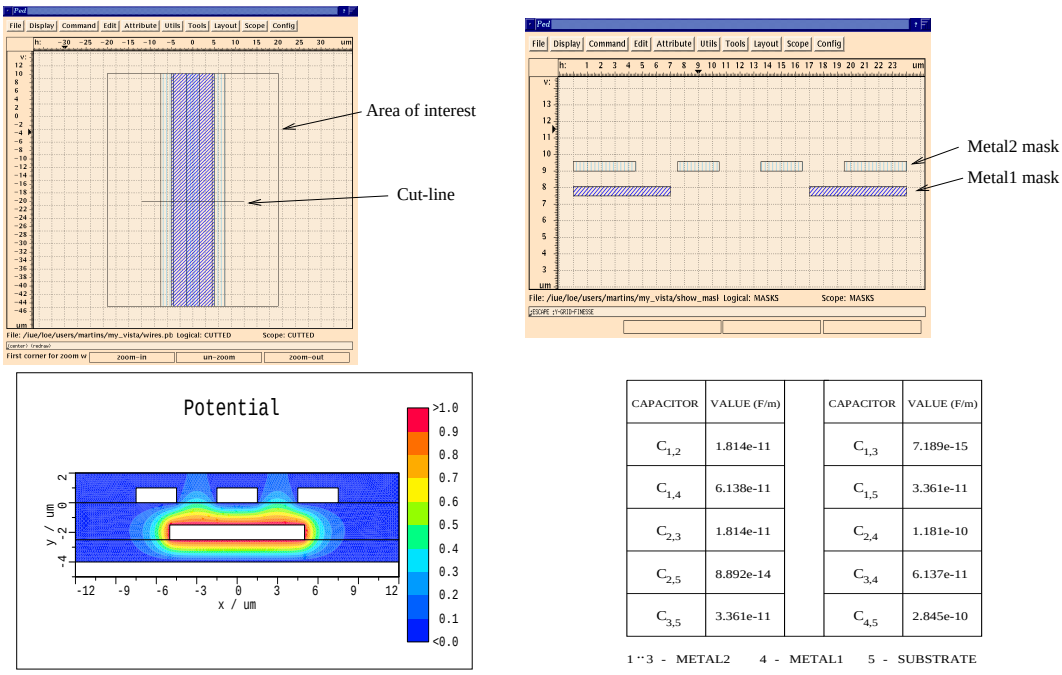

CAPACITOR	VALUE (F/m)		CAPACITOR	VALUE (F/m)
$C_{1,2}$	1.814e-11		$C_{1,3}$	7.189e-15
$C_{1,4}$	6.138e-11		$C_{1,5}$	3.361e-11
$C_{2,3}$	1.814e-11		$C_{2,4}$	1.181e-10
$C_{2,5}$	8.892e-14		$C_{3,4}$	6.137e-11
$C_{3,5}$	3.361e-11		$C_{4,5}$	2.845e-10

1 ··3 - METAL2 4 - METAL1 5 - SUBSTRATE

Figure 7: Interconnect capacitance extraction.

3 A New Diffusion Simulator PROMIS-NT

3.1 Introduction

The two-dimensional process simulator PROMIS-NT has been successfully implemented in the VISTA framework. It is possible with PROMIS-NT to solve now diffusion problems on arbitrary simulation domains. Therefore, PROMIS-NT fulfills the following needs:

- arbitrary, nonplanar and multilayered simulation structure
- flexible model initialization on different materials
- flexible modeling interface for the development of new models
- modeling environment for material interfaces
- numerical stability

An efficient grid generation module ensures the approximation of nonplanar geometries by using triangular grids. For multilayer simulations it is necessary to split up the overall grid into several material segment related grids.

It is possible to initialize different diffusion models for each material segment by using the segment grids. The basic idea is to decide whether to use a simple or an advanced diffusion model for the different materials. It makes no sense to use, e.g., point defect diffusion models on the whole simulation domain, hence each material should get its appropriate diffusion model. Additionally, a modeling interface for the implementation of new models must be provided for advanced users. A library of pre-defined models and temperature modes have to be provided for those users who are not interested in model development and only want to use the simulator's tuned built-in models.

Interface models can be chosen for the different adjacent material segments. Thereby a relation for the dopant concentrations on either side of the material interface is specified.

From the numerical point of view, several operations like adaptive gridding, equation solutions, time stepping, are done automatically by PROMIS-NT. This is a prerequisite for the usage of the simulator within a process flow.

3.2 Assembling the Diffusion Models

A flexible procedural modeling interface allows the specification of nearly any diffusion problem. Generally, different diffusion models can be specified on a given material segment. The user can specify the appropriate segment model from a library of pre-defined models. These pre-defined models contain no hard-coded modeling parameters, e.g. diffusion coefficient, solid solubility, the parameters are given via the procedural interface as input parameters.

Any specified model needs certain input data for being successfully evaluated. For example, if a point defect model should be applied to a silicon material segment, there must be silicon interstitials and vacancies available for the model setup. We have implemented an initialization function where the given input can be corrected, if necessary.

The structure of the implemented general diffusion equation which can be treated by PROMIS-NT is given by (1), where α and γ are prefactors determining the coupling between the quantities C_k.

$$\alpha_k \cdot \frac{\partial C_k}{\partial t} = -\operatorname{div} \vec{J_k} + \sum_{m=1}^{N_{max}} \gamma_{km} \quad k = 1 \cdots N_Q \tag{1}$$

$$\vec{J_k} = -D_k \cdot \operatorname{grad} C_k \tag{2}$$

$$\vec{J_k} = -D_k \cdot \operatorname{grad} C_k - Z \cdot C \cdot \mu \cdot \operatorname{grad} \psi \tag{3}$$

$$\vec{J_k} = f(D_k, C_k, \operatorname{grad} C_k, C_{net}, T, t) \tag{4}$$

It is possible to define N_{max} generation/recombination terms γ_{km} for each equation. The diffusion flux $\vec{J_k}$ can be specified from predefined models (2) - (3). By using a field enhancement model (3) only the diffusion coefficient D_k needs to be specified, the electrostatic potential ψ as well as the additional drift flux are calculated automatically. Furthermore, there can be any diffusion current model designed which depends on the parameters shown by (4).

If no special boundary conditions are specified for the diffusion equation, homogeneous Neumann boundary conditions (5) are assumed for all dopants at the outer geometry boundaries. Between the material interfaces one of the pre-defined interface models be chosen.

$$\vec{J} \cdot \vec{n} = 0 \tag{5}$$

With a flexible modeling interface it is possible to specify the parts of the generic diffusion equation (1) which should be used on a given material segment. The structures of the diffusion equations including all modeling functions are entered in modeling tables, which are taken by the *Universal Function Generator* (UNFUG) [2] to be considered during the source code generation of the core initialization routines.

After defining the models for each solution variable, including the interface models and the boundary conditions, the internal representation of the physical models are built up. Thereby the model information from all equations is combined to one single-linked list of simulation models. Figure 8 outlines the structure of this model list. Each entry holds the whole information about the involved quantities, the physical parameters and the grid information in its own data structure.

Once the model list is defined, it is kept constant during the whole simulation. The model queue is evaluated during the assembly of the linear system. Thereby the information in the model entries are used to apply the discretization scheme to the different parts of the diffusion equation.

3.3 Diffusion Model Library

As all of the following diffusion current models are using diffusivities, we first summarize available diffusion coefficients models. The diffusion coefficient D can modeled as follows:

$$D = D^{eq} = D_0 \cdot \exp\left(-\frac{E_0}{kT}\right) \tag{6}$$

$$D = D^{eq} \cdot [1 - \exp(t/\tau_0)] \tag{7}$$

$$D = \sum_{i=-r}^{r} D_i \cdot \exp\left(-\frac{E_i}{kT}\right) \cdot \left(\frac{n}{n_i}\right)^i \tag{8}$$

$$D = D^{eq} \cdot (f_I \cdot \frac{C_I}{C_I^{eq}} + f_V \cdot \frac{C_V}{C_V^{eq}}) \tag{9}$$

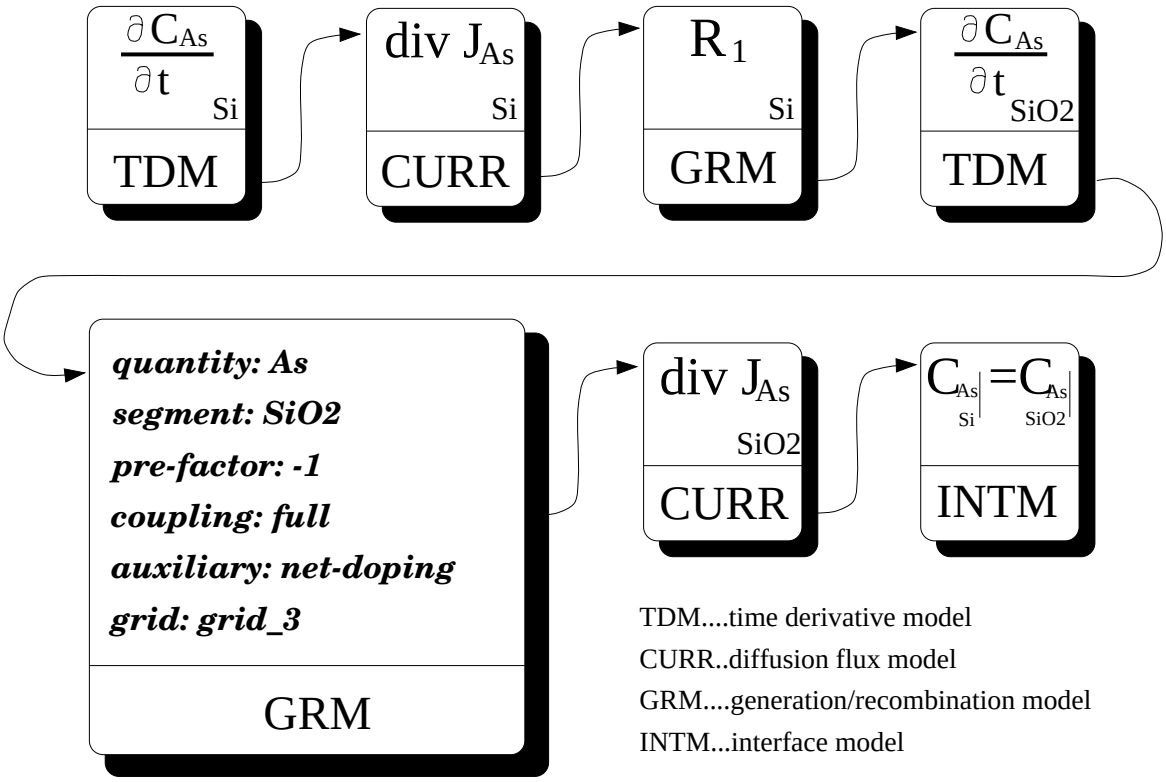

Figure 8: Internal model list representation for the diffusion equations of arsenic specified on two different material segments.

(6) gives the diffusivity D^{eq} at intrinsic doping conditions, where (7) is appropriate to model the diffusion in silicon dioxide, based on a temperature dependent diffusivity. Equation (8) refers to the extrinsic dopant diffusion, where different charge states of dopants are encountered. The same diffusion coefficient is also taken for multiply charged dopant/defect pairs. If the dopant diffusion is driven by excess point defect concentrations, the diffusion coefficient is extended as depicted by (9), where f_I and f_V are weighting factors representing the interstitial and vacancy diffusion mechanism, respectively.

Currently, the following diffusion models are implemented into PROMIS-NT and can be specified on the material segments:

- Coupled and uncoupled diffusion model
- Static and dynamic clustering model
- Transient enhanced diffusion model
- Transient activation model
- Polysilicon diffusion model

Details on the structure of the available diffusion models as well as model parameters and their validity for the above models can be found in [3].

For the material interfaces between different material segments the following interface models are available:

- Conduction model
- Segregation model
- Polysilicon/Silicon interface model

3.4 User Interface

Two possibilities are offered within the VISTA framework to run PROMIS-NT. First, as single step tool using a user interface panel (see. Fig 9) to start the simulator. Thereby, the input PIF file and the input simulation grid can be specified. If the input simulation grid is not valid (e.g. an ortho-product grid specified on a nonplanar structure) an own simulation grid is generated and the available quantities are interpolated to this new grid. Additionally, this grid is adapted according the input quantities to resolve them adequately.

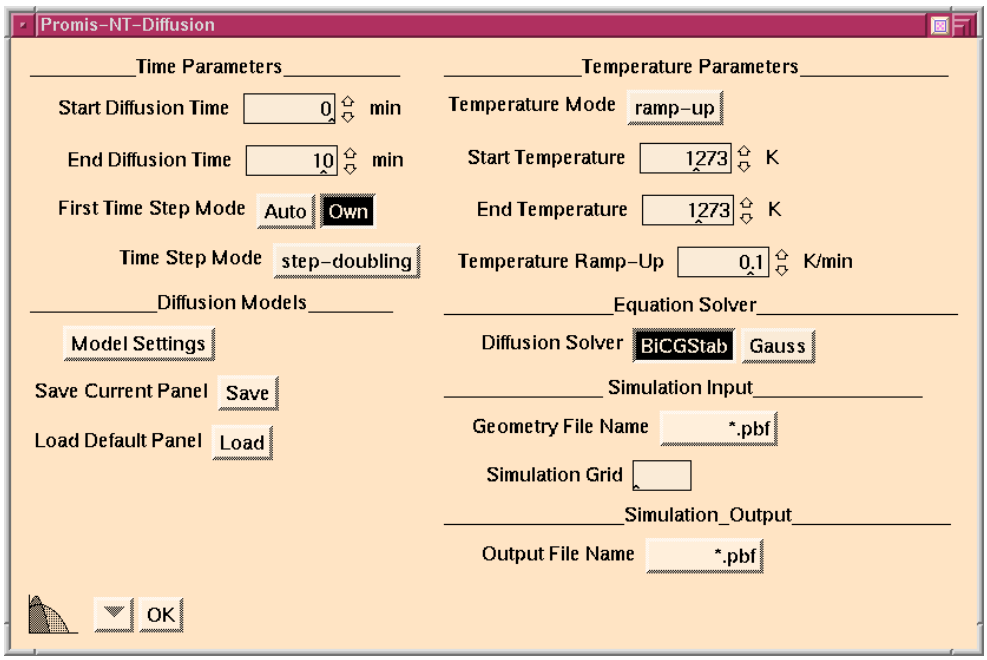

Figure 9: User interface panel for PROMIS-NT

Furthermore, the physical diffusion parameters like temperature and annealing time can be specified. For the specification of the diffusion model on a given material segment the model definition panel (see Fig 10) is used. It is even possible to disable the diffusion equations on material segments which are less critical. In this case the initial concentrations are written unchanged to the output file.

Secondly, PROMIS-NT operates in the library of process simulation tools of VISTA's Simulation Flow Control (SFC). Thereby, the models and the physical parameters can be specified by the user. Input data are automatically given by the previous simulation step and output date are delivered to the next simulation tool.

3.5 Example – BiCMOS Process Simulation

As an example, a complete $0.8\mu m$ BiCMOS process [4] was simulated with VISTA's *Simulation Flow Controller* (SFC) [5], using PROMIS-NT as diffusion simulator.

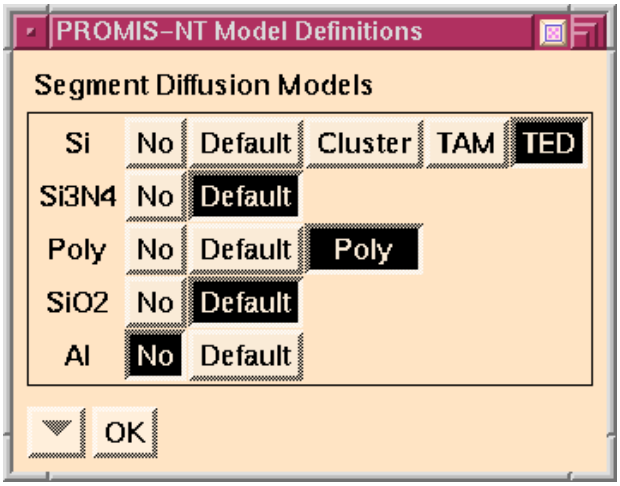

Figure 10: User interface panel for the specification of the segment models

A tabularized process flow including all process parameters is given in Table 1. Each step of the flow represents a process simulation tool which reads the last result from the previous one and performs the simulation according to the specifications. After the tool has finished, the actual wafer state is evaluated. This includes merging of the geometry and the doping information.

The following process simulation tools are available in the SFC:

SKETCH**:** Simulation module for resist spin-on, exposure, and stripping.

PROMIS**:** Process simulation modules for several steps:

- ETCH: Etching tool for isotropic, anisotropic and plasma etching [6].
- DEPO: Deposition tool for isotropic, anisotropic and hemispherical deposition of material layers. Additionally, EPI-layer deposition and *in-situ* doping techniques are performed.
- ANALYTICAL IMPLANT: Ion implantation module based on analytic distribution function.
- DIFFUSION: Diffusion in silicon (obsolescent).
- MONTE CARLO IMPLANT: Ion implantation module based on Monte Carlo technique. Available for amorphous as well as crystalline targets.

PROMIS-NT**:** Simulation module for diffusion processes.

SAMPLE**:** Etching and deposition module incorporated by a wrapper approach [7].

TSUPREM-4**:** Process simulator for diffusion, oxidation, implantation [8].

A schematic cross-section of the BiCMOS structure is shown in Figure 11. The final BiCMOS structure is given in Figure 12. Figure 13 shows the actual dopant concentrations after the channel-stop implant (step 31) prior to the field oxide isolation, where the n-wells and the p-well doping concentrations are also given. The active region of the NPN device including extrinsic base, intrinsic base and emitter doping is shown in Figure 14. Details of the corresponding simulation grid are depicted in Figure 15.

#	Simulator	SFC operation	Specification & Parameters
1	SKETCH	create-subdomain	create wafer: Si, p-type $10\Omega cm$ $22.0 \times 5.0\mu m$
2	SKETCH	spin-on	pad oxide: SiO_2, $0.025\mu m$
3	SKETCH	spin-on	nitride buffer: Si_3N_4, $0.3\mu m$
4	SKETCH	mask	pattern buried layers: exposed, mask: 7.0, 13.5; 14.5, 22.0;
5	PROMIS	etch	open nitride
6	SKETCH	strip-material	mask
7	PROMIS	analytic-implant	N-buried layer: Sb, $200keV$, $110^{15}cm^{-2}$
8	TSUPREM-4	oxidation	oxidation: SiO2, $0.5\mu m$, 1200C $100min$ dry O_2, 1100C $35min$ wet O_2
9	SKETCH	strip-material	strip mask: resist
10	PROMIS	analytic-implant	P-buried layer: B, $75keV$, $110^{15}cm^{-2}$
11	SKETCH	strip-material	strip oxide: $SiO2$
12	PROMIS	iso-depo	epi layer: Si $1.6\mu m$, in-situ P $110^{15}cm^{-2}$
13	PROMIS	iso-depo	pad oxide: SiO_2 $500\AA$
14	PROMIS	iso-depo	nitride buffer: Si_3N_4 $0.3\mu m$
15	SKETCH	mask	pattern N-well: exposed, mask: 7.0, 13.5; 14.5, 22.0;
16	PROMIS	etch	open nitride
17	SKETCH	strip-material	mask
18	PROMIS	analytic-implant	N-well: P, $150keV$, $210^{12}cm^{-2}$
19	TSUPREM-4	oxidation	oxidation: SiO2, $0.3\mu m$, 1200C $10min$ dry O_2 , 1100C $25min$ wet O_2
20	SKETCH	strip-material	strip resist
21	PROMIS	analytic-implant	P-well: B, $55keV$, $810^{12}cm^{-2}$
22	PROMIS-NT	diffusion	well drive-in: 1000C $150min$
23	PROMIS	iso-etch	planarize
24	SKETCH	spin-on	pad oxide: SiO_2, $300\AA$
25	SKETCH	spin-on	poly buffer: poly $500\AA$
26	SKETCH	spin-on	nitride buffer: Si_3N_4, $1.0\mu m$
27	SKETCH	mask	pattern field oxide: exposed, mask: 0.0 ,0.5; 6.5, 7.5; 13.5, 14.5; 19.5, 20.2; 21.8, 22.0;
28	PROMIS	etch	open nitride
29	SKETCH	strip-material	mask
30	PROMIS	plasma-etch	open channel stop
31	PROMIS	analytic-implant	channel stop: B, $30keV$, $210^{13}cm^{-2}$
32	TSUPREM-4	oxidation	field oxide: 975C, $150min$
33	SKETCH	strip-material	strip nitride

#	Simulator	SFC operation	Specification & Parameters
34	SKETCH	mask	pattern subcollector: exposed, mask: 20.5,21.5;
35	PROMIS	analytic-implant	N+ subcollector: P, $180keV$, $210^{15}cm^{-2}$
36	SKETCH	strip-material	strip resist
37	SKETCH	mask	pattern base: exposed, mask: 14.8,19.2
38	PROMIS	analytic-implant	intrinsic base: B, $25keV$, $210^{13}cm^{-2}$
39	PROMIS	iso-depo	deposit: SiO_2, $0.16\mu m$
40	SKETCH	strip-material	strip resist
41	PROMIS	iso-etch	pregate oxide
42	PROMIS	iso-depo	gate oxide: SiO_2, $0.02\mu m$
43	SKETCH	mask	pattern open emitter: mask: 17.6,18.4;
44	PROMIS	plasma-etch	open emitter
45	SKETCH	strip-material	strip resist
46	PROMIS	iso-depo	poly deposit: poly $0.25\mu m$
47	PROMIS	analytic-implant	N+ gate/emitter implant: As, $60keV$, $210^{16}cm^{-2}$
48	SKETCH	mask	pattern emitter/gate: mask: 0.0, 3.1; 3.9, 10.1; 10.9, 17.1; 18.9, 22.0;
49	PROMIS	etch	form gates and emitter
50	SKETCH	mask	pattern S/D + deep collector: mask: 0.0,5.5; 7.5, 8.5;20.5,21.5;
51	PROMIS	analytic-implant	NMOS LDD S/D implant: P, $40keV$, $310^{13}cm^{-2}$
52	SKETCH	strip-material	strip resist
53	PROMIS	iso-depo	deposit sidewall spacer oxide $0.27\mu m$
54	PROMIS	iso-etch	sidewall etch $0.3\mu m$
55	SKETCH	mask	pattern S/D + deep collector: mask: 0.0,5.5; 7.5, 8.5;20.5,21.5;
56	PROMIS	analytic-implant	NMOS S/D implant: P, $60keV$, $410^{15}cm^{-2}$
57	SKETCH	strip-material	strip resist
58	SKETCH	mask	pattern PMOS S/D + extr. base: mask: 5.5, 7.0; 8.5, 17.0
59	PROMIS	analytic-implant	PMOS S/D + extr. base: B, $25keV$, $310^{15}cm^{-2}$
60	SKETCH	strip-material	strip resist
61	PROMIS-NT	diffusion	S/D - emitter: 1050C, $15s$

Table 1: Process simulation flow for the $0.8\mu m$ BiCMOS process.

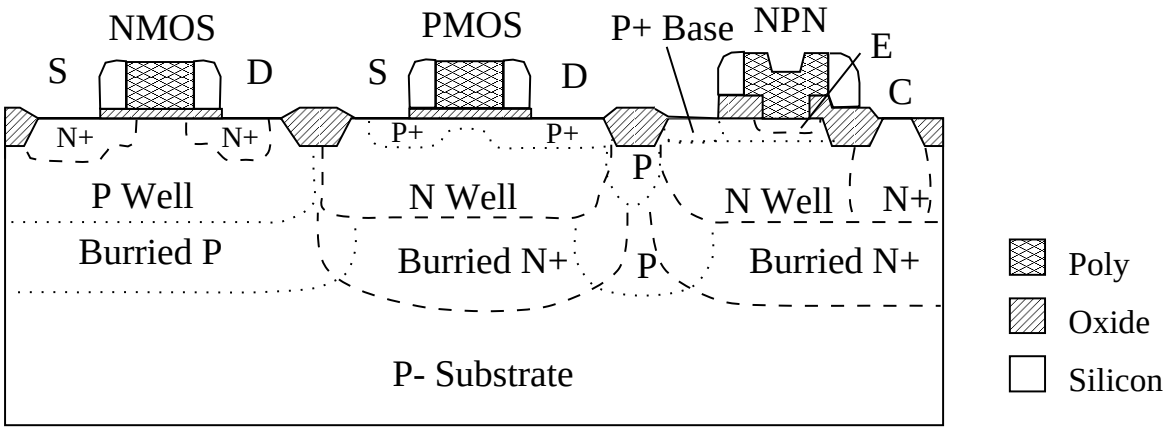

Figure 11: Device cross-section of BiCMOS process after fabrication of the active areas. The source–drain anneal is optimized to emitter outdiffusion conditions. Afterwards the structure is scheduled for a double-level interconnect process.

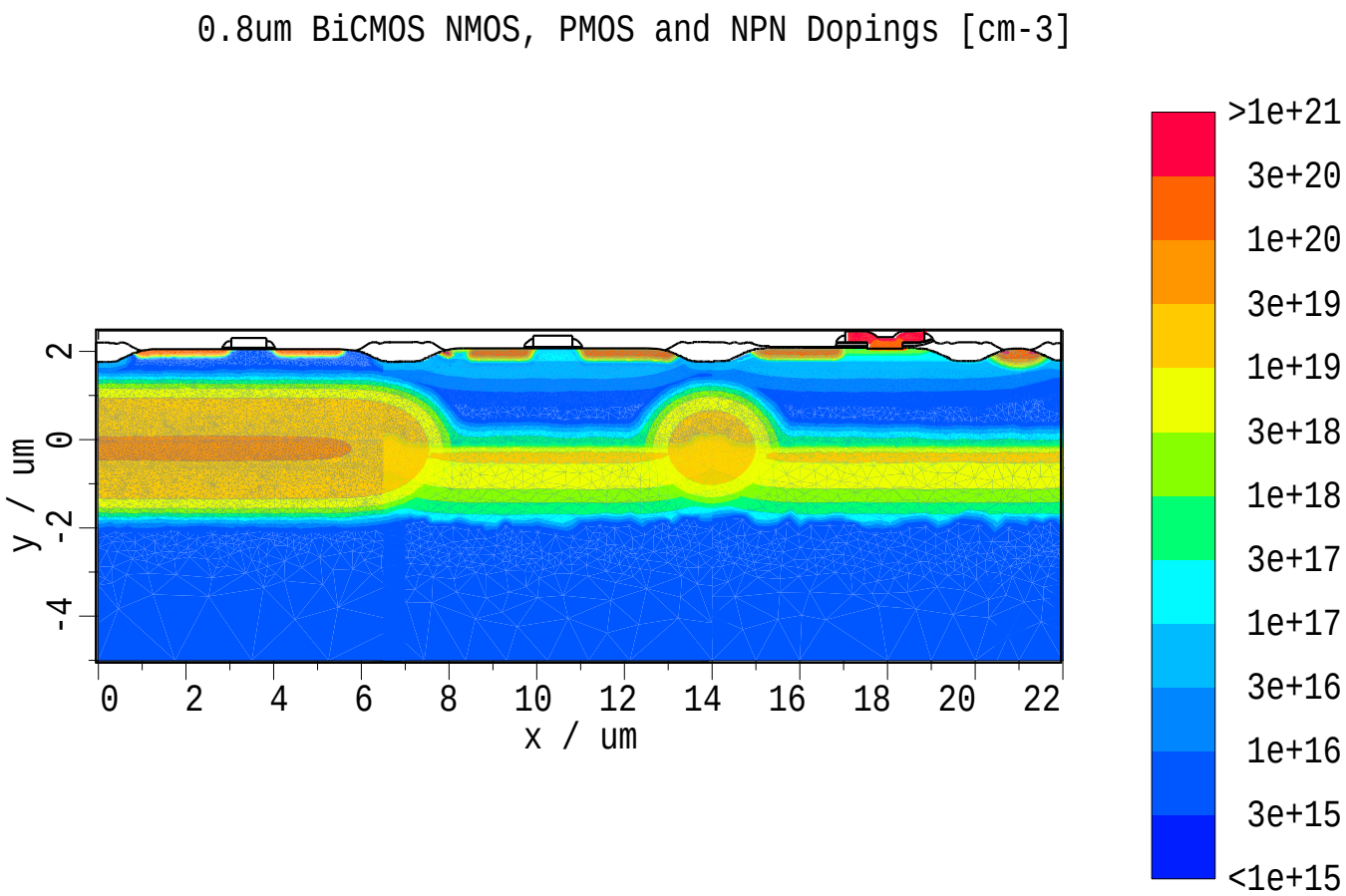

Figure 12: Simulation results for the final BiCMOS device including NMOS, PMOS and NPN dopings.

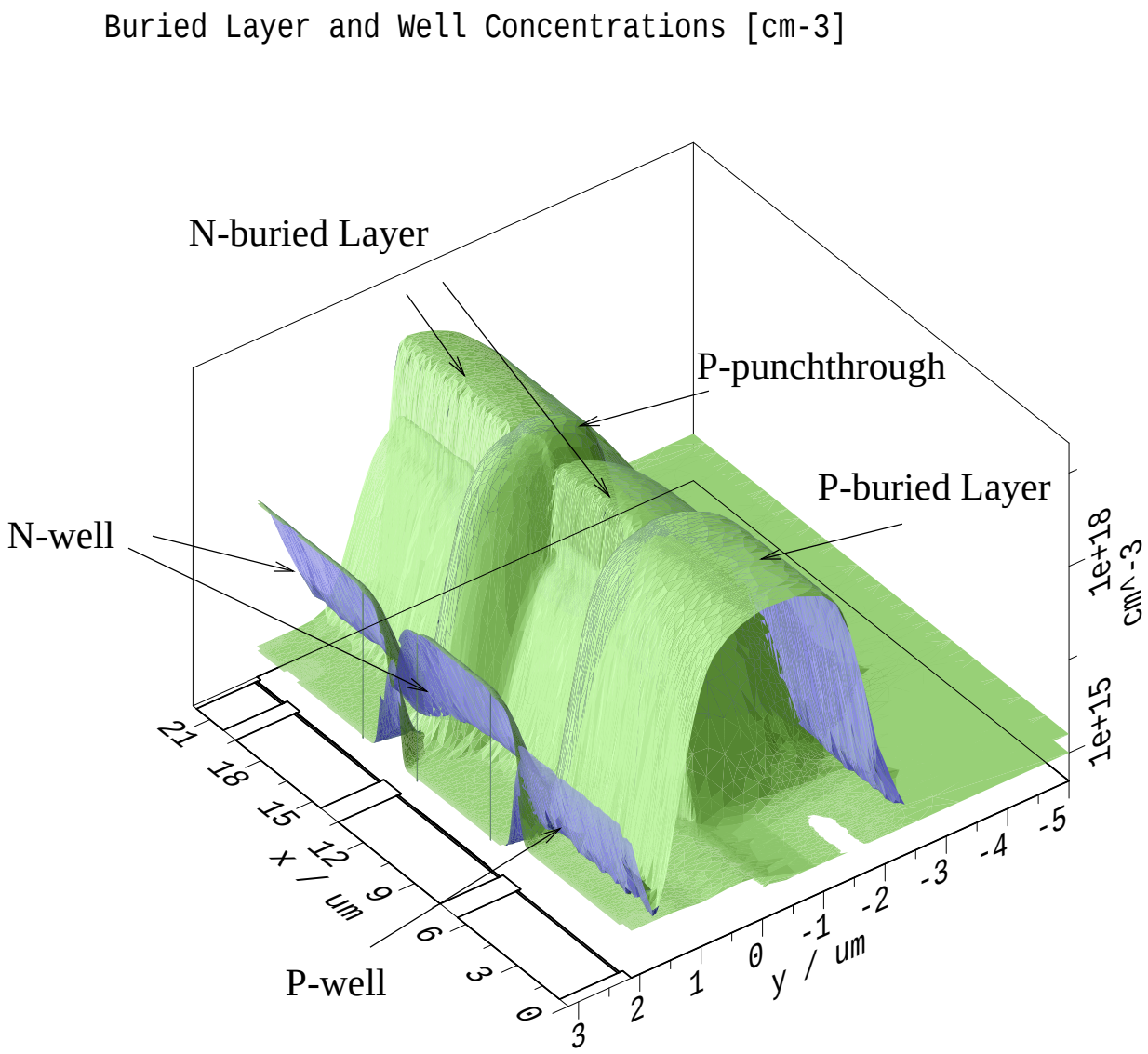

Figure 13: Simulation results for the P-buried layer, the P-punchthrough and the N-buried layers obtained after step 31.

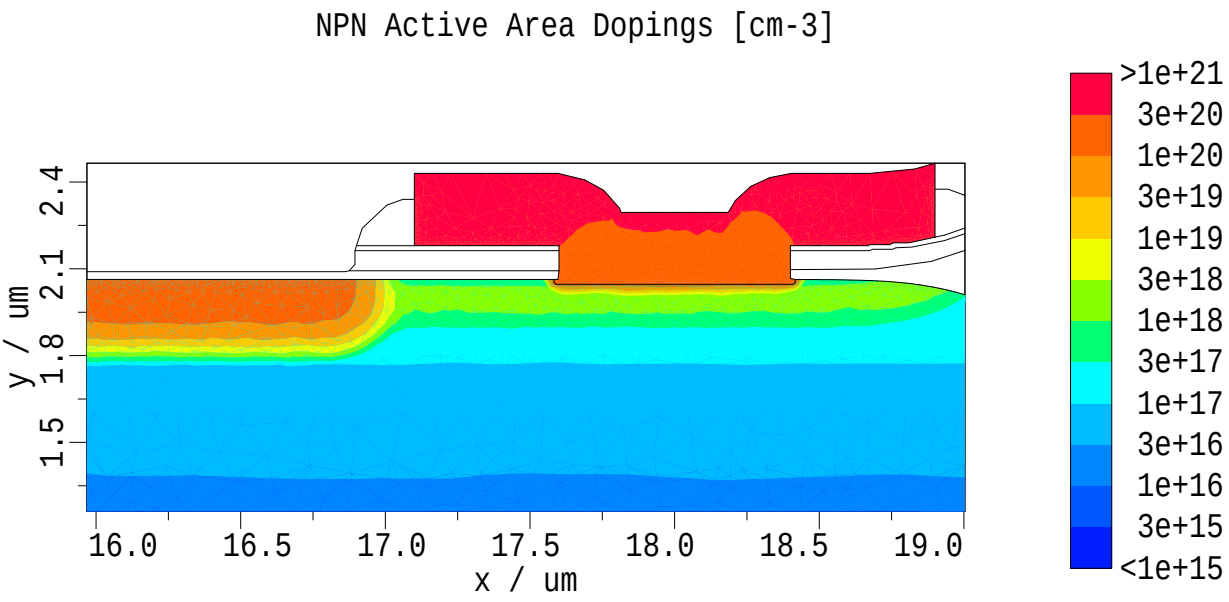

Figure 14: The active area of the NPN device showing intrinsic and extrinsic base, emitter and collector.

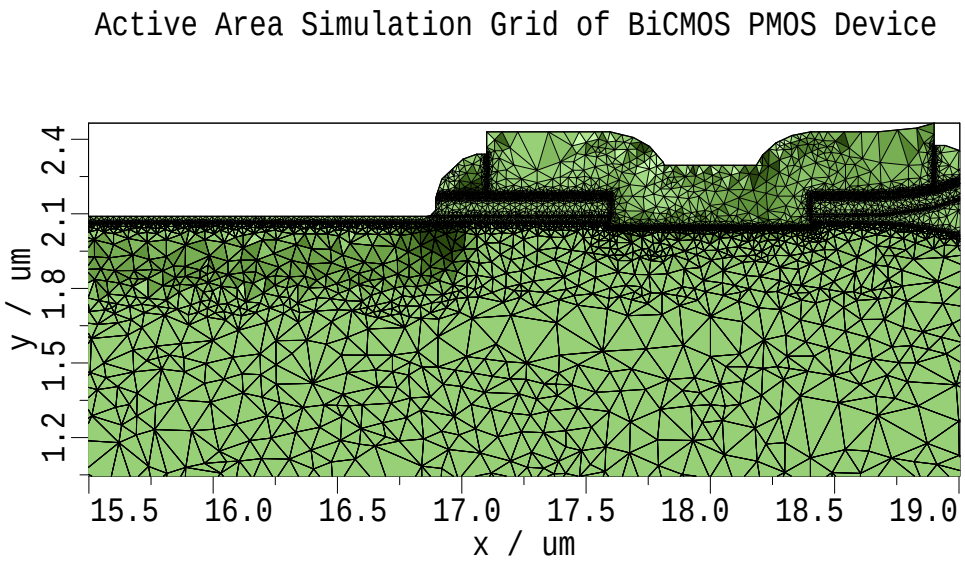

Figure 15: Details on the simulation grid of the active area for the NPN device.

4 Simulation of Submicron Double-Heterojunction High Electron Mobility Transistors with MINIMOS-NT

4.1 Introduction

In recent years, high electron mobility transistors (HEMTs) have become a widely used supplement to the spectrum of industrial semiconductor devices. Especially pseudomorphic submicron HEMTs have conquered a broad field of application because of their high-frequency performance. The DC characteristics of a pseudomorphic double-heterojunction AlGaAs/InGaAs HEMT with a gate length of $240\ \mathrm{nm}$ are investigated by two-dimensional device simulation with MINIMOS-NT using the capabilities of the VISTA framework. The simulation results are compared with measured data and three distinct operation regimes of the transfer characteristics can be diagnosed, each owing to a major physical effect. Identifying the essential physical mechanisms which are responsible for particular effects of the HEMT's electrical behavior by means of simulation allows to push ahead the further development of HEMTs. The capability of simulation includes device scaling as well as the potential of band gap engineering. Both improvements can be realized by process technology due to advances in epitaxial growth producing epilayers of almost arbitrary material composition.

The simulation of HEMTs is mainly facing two problems. Of concern are short channel effects caused by reducing the gate length well below a quarter micron. Secondly, the device characteristics strongly depend on the properties of abrupt heterojunction interfaces.

To account for short channel effects several attempts have been made to make the hydrodynamic (HD) model suitable for device simulation [9]-[12]. However, the convergence of the HD model is weak and the computational effort is high, since the set of unknowns is augmented by the carrier energies. Both effects can be mitigated when the HD model is only used for regions of the device where non-local behavior is dominating, hence by mixing drift-diffusion (DD) and hydrodynamic model (mixed model simulation). For HEMTs the critical region is the channel layer. To apply the HD model only for the channel layer, this region must be cut out and then linked with the remaining regions by specific interface models. Thus, the device region is split into a set of subdomains by a process referred to as segment split method (SSM) [13].

Moreover, the SSM offers an elegant way to handle abrupt heterojunctions using specific interface models mentioned above. Previously published simulators are only capable of dealing with continuous material properties [14][15] and therefore ignoring thermionic-field emission, or they are designed for only one dimension in space [16][17]. Using SSM it is possible to combine models for abrupt heterojunctions and two-dimensional device simulation. Accordingly, for the simulation of HEMTs the short channel effects can be considered as well as the influence of the thermionic-field emission on the confinement of the electrons inside the channel layer.

In Section 4.2 the equations for the drift-diffusion and hydrodynamic models, the interface model for thermionic-field emission, and the physical models are presented along with some notes on numerics. The measured DC characteristics are compared with simulation results in Section 4.7 as well as a discussion of several physical effects which influence the transfer characteristics. Finally, some conclusions are presented in Section 4.8.

4.2 Segment Split Method and Mixed Drift-Diffusion Hydrodynamic Simulation

The electrical behavior of the HEMT is mainly determined by the epitaxial grown structure of the device. Several distinct layers of different semiconductor alloys are combined to obtain a channel with high

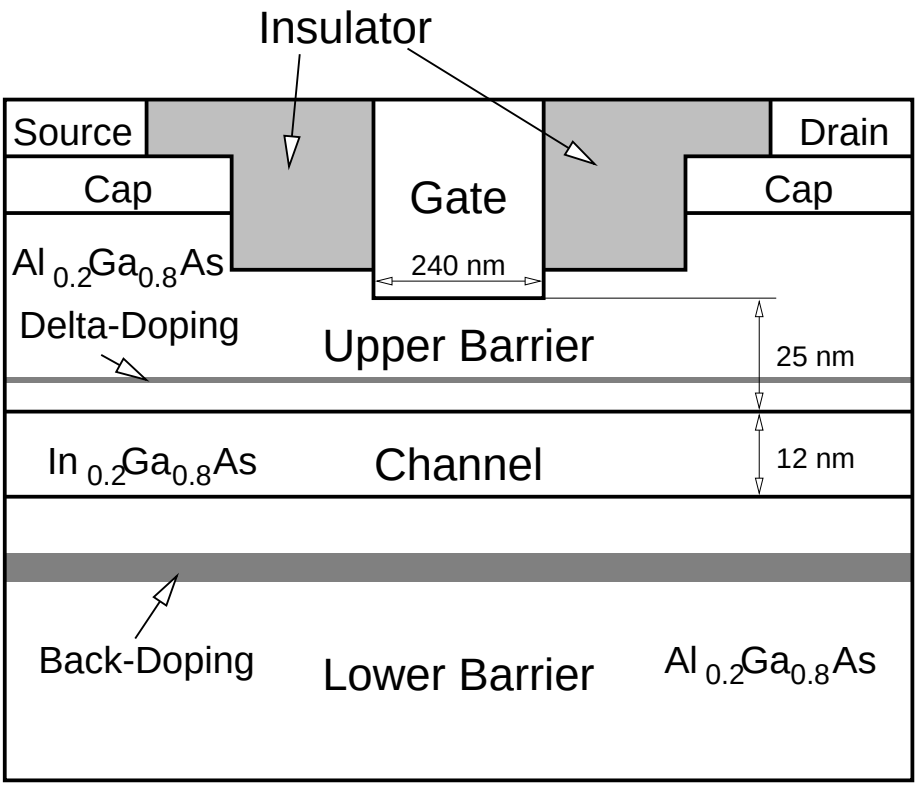

Figure 16: Schematic cross section of a delta-doped pseudomorphic double-heterojunction HEMT. The current is conducted inside the narrow band-gap $\mathrm{In_{0.2}Ga_{0.8}As}$ channel layer, $12\ \mathrm{nm}$ thick, which is sandwiched between the wide band-gap $\mathrm{Al_{0.2}Ga_{0.8}As}$ upper and lower barrier layer. The device structure is built with the SFC tool of the VISTA framework.

electron mobility and high electron concentration. The properties of the channel are expected to govern the electron transport (see Fig. 16). The material and electrical properties change almost abruptly at the heterojunction interfaces, i.e., at interfaces between different layers. Inside a layer the material properties and the electrical quantities are continuous, and the partial differential equations (PDE) describing the electrical behavior can be solved numerically. The discontinuous behavior on interfaces between layers has to be treated by specific interface models to link the layers together. For the simulation the device domain is split into several subdomains, referred to as segments. Each segment corresponds to a distinct layer of the device. This process is termed segment split method (SSM).

Abrupt heterojunction interfaces can be properly handled with interface models. Especially, the effects of tunneling through energy barriers at heterojunction interfaces can be considered analytically for arbitrary device geometries. Tunneling is important to describe the electron transport from the drain-sided end of the channel into the barrier layer above. Furthermore, by linking segments with different properties by appropriate interface models, the models for the segments can also be different. Thus, for the channel segment a five equation hydrodynamic (HD) model can be used to account for short channel effects and a plain three equation drift-diffusion (DD) model for the other segments. Compared to simulations using the HD model for the entire device, mixed DD/HD model simulations are more effective with respect to computation time and the convergence of the iteration scheme.

4.3 Basic Equations

In the following the basic equations used for the simulation of the HEMT are given. For plain drift-diffusion modeling the well known Poisson equation and continuity equations are used. Additionally, to account for short channel effects, a hydrodynamic model describing the energy transport is implemented and the continuity equations are extended for non-constant carrier temperatures.

The Poisson and continuity equations read

$$\nabla(\varepsilon \cdot \nabla\psi) - q \cdot (n - p + N_A^- - N_D^+ - N_{DD}^+) = 0 \tag{10}$$

$$\nabla\vec{J}_\mathrm{n} - q \cdot \frac{\partial n}{\partial t} - q \cdot R = 0 \tag{11}$$

$$\nabla\vec{J}_\mathrm{p} + q \cdot \frac{\partial p}{\partial t} + q \cdot R = 0 \tag{12}$$

where $\vec{J}_\mathrm{n}$ and $\vec{J}_\mathrm{p}$ are the electron and hole current densities, respectively, R is the net recombination rate, ε is the permittivity, n and p the electron and hole concentrations, q is the absolute electron charge, N_A^- and N_D^+ are the densities of ionized acceptors and donors, and N_{DD}^+ is the density of ionized deep traps, respectively.

The current densities are defined as

$$\vec{J}_\mathrm{n} = q \cdot \mu_\mathrm{n} \cdot n \cdot \left[\nabla\left(\frac{E_C}{q} - \psi\right) + \frac{k}{q} \cdot \frac{N_C}{n} \cdot \nabla\frac{n \cdot T_\mathrm{n}}{N_C}\right] \tag{13}$$

$$\vec{J}_\mathrm{p} = q \cdot \mu_\mathrm{p} \cdot p \cdot \left[\nabla\left(\frac{E_V}{q} - \psi\right) - \frac{k}{q} \cdot \frac{N_V}{p} \cdot \nabla\frac{p \cdot T_\mathrm{p}}{N_V}\right], \tag{14}$$

where the non-constant carrier temperatures and effective-density-of-states are considered by the terms $\nabla\frac{n \cdot T_\mathrm{n}}{N_C}$ and $\nabla\frac{p \cdot T_\mathrm{p}}{N_V}$, respectively. The terms $\nabla\left(\frac{E_C}{q} - \psi\right)$ and $\nabla\left(\frac{E_V}{q} - \psi\right)$ account for the non-constant band edge energies. The definition of the carrier mobilities μ_n and μ_p depends on the applied model and considers a field dependence for the DD model and a carrier temperature dependence for the HD model.

For the HD model the equations governing the energy transport are

$$\begin{aligned}\nabla\vec{S}_\mathrm{n} + \frac{\partial(n \cdot w_\mathrm{n})}{\partial t} - \nabla\left(\frac{E_C}{q} - \psi\right) \cdot \vec{J}_\mathrm{n} + \\ + n \cdot \frac{w_\mathrm{n} - w_0}{\tau_{wn}} + w \cdot R = 0\end{aligned} \tag{15}$$

$$\begin{aligned}\nabla\vec{S}_\mathrm{p} + \frac{\partial(p \cdot w_\mathrm{p})}{\partial t} - \nabla\left(\frac{E_V}{q} - \psi\right) \cdot \vec{J}_\mathrm{p} + \\ + p \cdot \frac{w_\mathrm{p} - w_0}{\tau_{wp}} + w \cdot R = 0\end{aligned} \tag{16}$$

where

$$\vec{S}_\mathrm{n} = -\kappa_\mathrm{n} \cdot \nabla T_\mathrm{n} - \frac{1}{q} \cdot (w_\mathrm{n} + k \cdot T_\mathrm{n}) \cdot \vec{J}_\mathrm{n} \tag{17}$$

$$\vec{S}_\mathrm{p} = -\kappa_\mathrm{p} \cdot \nabla T_\mathrm{p} + \frac{1}{q} \cdot (w_\mathrm{p} + k \cdot T_\mathrm{p}) \cdot \vec{J}_\mathrm{p} \tag{18}$$

are the electron and hole energy fluxes, respectively, τ_{wn} and τ_{wp} are the energy relaxation times, and w_n and w_p are the electron and hole energies, respectively. Since the simulations are performed for room

temperature $T = 300$ K the drift kinetic energy part is small compared to the random kinetic energy of the carriers and can be neglected

$$w_{\mathrm{n,p}} \approx \frac{3}{2} \cdot k \cdot T_{\mathrm{n,p}}. \tag{19}$$

For the thermal conductivities the Wiedemann-Frantz-Law is used

$$\kappa_{\mathrm{n,p}} = \frac{5}{2} \cdot \frac{k^2}{q} \cdot T_{\mathrm{n,p}} \cdot \mu_{\mathrm{n,p}} \cdot (n, p). \tag{20}$$

Furthermore, for the discretization of the continuity and energy balance equations we implemented the scheme proposed in [11] to improve the weak convergence behavior of the HD model.

4.4 Interface Models

Considering the interface between segment 1 and segment 2 the thermionic-field emission model determines the electron current density J_{n1} leaving segment 1, the electron current density J_{n2} entering segment 2, the electron energy flux density S_{n1} leaving segment 1, and the electron energy flux density S_{n2} entering segment 2:

$$J_{\mathrm{n2}} = J_{\mathrm{n1}}, \tag{21}$$

$$S_{\mathrm{n2}} = S_{\mathrm{n1}} + \frac{1}{q} \cdot (\Delta E_C - \delta E_C) \cdot J_{\mathrm{n2}} \tag{22}$$

$$\begin{aligned} J_{\mathrm{n2}} &= q \cdot v_{\mathrm{n2}}(T_{\mathrm{n2}}) \cdot n_2 - \\ &-q \cdot \frac{m_{\mathrm{n2}}}{m_{\mathrm{n1}}} \cdot v_{\mathrm{n1}}(T_{\mathrm{n1}}) \cdot n_1 \cdot \exp\left(-\frac{\Delta E_C - \delta E_C}{k \cdot T_{\mathrm{n1}}}\right), \end{aligned} \tag{23}$$

$$\begin{aligned} S_{\mathrm{n2}} &= -2 \cdot k \cdot T_{\mathrm{n2}} \cdot v_{\mathrm{n2}}(T_{\mathrm{n2}}) \cdot n_2 + \\ &+2 \cdot \frac{m_{\mathrm{n2}}}{m_{\mathrm{n1}}} \cdot k \cdot T_{\mathrm{n1}} \cdot v_{\mathrm{n1}}(T_{\mathrm{n1}}) \cdot n_1 \cdot \exp\left(-\frac{\Delta E_C - \delta E_C}{k \cdot T_{\mathrm{n1}}}\right), \end{aligned} \tag{24}$$

where

$$v_{\mathrm{n1,2}}(T_{\mathrm{n1,2}}) = \sqrt{\frac{2 \cdot k \cdot T_{\mathrm{n1,2}}}{\pi \cdot m^*_{\mathrm{n1,2}}}} \tag{25}$$

denotes the "emission velocity", and $m^*_{\mathrm{n1,2}}$ are the electron effective masses for segments 1 and 2, respectively. The barrier height is defined as

$$\Delta E_C = E_{C2} - E_{C1}. \tag{26}$$

For the electrostatic potential the interface condition reads

$$\psi_1 = \psi_2. \tag{27}$$

Tunneling of electrons through the energy barrier is taken into account by barrier height lowering, which is modeled as

$$\delta E_C = \begin{cases} q \cdot E_\perp \cdot x_{\mathrm{eff}}, & E_\perp > 0 \\ 0, & E_\perp \leq 0 \end{cases} \tag{28}$$

where $E_\perp$ is the electric field perpendicular to the interface in segment 2 and x_{eff} is the effective tunnel length which is assumed with 7 nm.

The exponential term in eq. (23) containing the barrier height determines the current flow across the interface. The effectiveness of this energy barrier is reduced either by barrier height lowering due to

tunneling or by increasing electron temperature T_{n1}. Thus, the carrier temperature influences the current flux across the interface – the higher the electron temperature the more electrons are able to surmount the energy barrier. This effect is referred to as real-space transfer (RST, [18]).

The mixed DD/HD model simulation requires a suitable value for the electron temperature T_{n2} inside the wide band-gap semiconductor segment where the carrier temperature is not calculated explicitly. One possibility is to assume the carrier temperature identical to the lattice temperature. However, full HD simulations show that the carrier temperature does not change very much in the vicinity of the interface. Thus, for mixed model simulation the carrier temperatures on both sides of the interface are supposed to be equal ($T_{n1} = T_{n2}$).

4.5 Numerical Methods

The discretized non-linear equation system is solved by a Newton-Raphson scheme. Additionally, to improve the well known weak convergence of the energy transport equations a block iterative scheme is implemented. First, the set of Poisson equation and continuity equations is solved alternately with the set of continuity equations and energy transport equations. Each set is solved iteratively by the Newton-Raphson method until the norm of the updates remains under a certain value. At last, for the full equation set the Newton-Raphson method [19][20] is invoked to obtain the desired final accuracy. The linear system is solved either by a Gauß-solver or by a state-of-the-art BiCGStab algorithm [21]. When the BiCGStab algorithm is employed, at first the matrix is scaled with an iterative algorithm [22] and preconditioned [23].

4.6 Physical models

In the sequel the models for the band edge energies [24], the electron and hole effective masses [24], and the mobilities for $\mathrm{Al_xGa_{1-x}As}$ and $\mathrm{In_yGa_{1-y}As}$ are given.

Usually, the band gap energies are used for simulation. However, the correct treatment of the abrupt heterojunctions requires the energy barrier height on the interfaces, i.e., the values for the conduction band edge energy and the valence band edge energy as well.

The band gap energy for $\mathrm{Al_xGa_{1-x}As}$ reads

$$E_g(x,T) = E_g(x,0) - \frac{\alpha(x)\cdot T^2}{\beta(x)+T}, \tag{29}$$

$$E_g(x,0) = E_g^{\mathrm{GaAs}}\cdot(1-x) + E_g^{\mathrm{AlAs}}\cdot x, \tag{30}$$

$$\alpha(x) = \alpha^{\mathrm{GaAs}}\cdot(1-x) + \alpha^{\mathrm{AlAs}}\cdot x, \tag{31}$$

$$\beta(x) = \beta^{\mathrm{GaAs}}\cdot(1-x) + \beta^{\mathrm{AlAs}}\cdot x, \tag{32}$$

where $E_g(x,T)$ is given in eV and T is the lattice temperature in K.

The band gap energy for InAs reads

$$E_g^{InAs}(T) = E_g^{\mathrm{InAs}} - \frac{\alpha^{\mathrm{InAs}}\cdot T^2}{\beta^{\mathrm{InAs}}+T}, \tag{33}$$

with the appropriate parameters E_g^{InAs}, α^{InAs}, and β^{InAs} (see Tab. 2).

The band gap energy for $\mathrm{In_yGa_{1-y}As}$ is given by

$$E_g(y,T) = E_g^{\mathrm{GaAs}}(T)\cdot(1-y) + E_g^{\mathrm{InAs}}(T)\cdot y - C\cdot y^2, \tag{34}$$

where $E_g^{\mathrm{GaAs}}(T)$ and $E_g^{\mathrm{InAs}}(T)$ are the band gap energies for Gallium-Arsenide and Indium-Arsenide, respectively, and C is the "bowing" parameter [24]. For the values of the parameters see Table 2.

Table 2: Parameter values for modeling the band gap energies.

α^{GaAs} [10^{-4}eV/K]	α^{AlAs} [10^{-4}eV/K]	α^{InAs} [10^{-4}eV/K]
5.58	8.78	2.76
β^{GaAs} [K]	β^{AlAs} [K]	β^{InAs} [K]
220	322	83
E_g^{GaAs} [eV]	E_g^{AlAs} [eV]	E_g^{InAs} [eV]
1.521	2.891	0.42
C [eV]	0.475	

The band gap energy is related to the band edge energies by

$$E_C(x,T) = E_g(0,T) + 0.6\cdot[E_g(x,T) - E_g(0,T)] \tag{35}$$

$$E_V(x,T) = E_C(x,T) - E_g(x,T), \tag{36}$$

thus, 60% of the change of the band gap energy are attributed to the conduction band edge energy and 40% to the valence band edge energy.

The carrier effective masses for $\mathrm{Al_xGa_{1-x}As}$ read

$$m^*_{\mathrm{n,p}} = m0_{\mathrm{n,p}} + m1_{\mathrm{n,p}}\cdot x + m2_{\mathrm{n,p}}\cdot x^2, \tag{37}$$

where for $x = 0$ the effective masses for GaAs are obtained. Table 3 shows the values used for these parameters.

Table 3: Parameter values for modeling the carrier effective masses.

Parameter	AlGaAs	InGaAs
$m0_{\mathrm{n}}$	$+0.067$	$+0.079$
$m1_{\mathrm{n}}$	$+0.083$	-0.038
$m2_{\mathrm{n}}$	–	–
$m0_{\mathrm{p}}$	$+0.080$	$+0.120$
$m1_{\mathrm{p}}$	$+0.080$	-0.099
$m2_{\mathrm{p}}$	–	$+0.030$

The carrier effective masses for $\mathrm{In_yGa_{1-y}As}$ are governed by

$$m^*_{\mathrm{n,p}} = m0_{\mathrm{n,p}} + m1_{\mathrm{n,p}}\cdot y + m2_{\mathrm{n,p}}\cdot y^2, \tag{38}$$

where the effective masses for InAs are obtained with $y = 1.0$ (see also Tab. 3).

The DD mobility is modeled by

$$\mu_{\mathrm{n,p}}(|\vec{F}_{\mathrm{n,p}}|) = \frac{\mu^0_{\mathrm{n,p}}}{\sqrt{1+\left(\frac{\mu^0_{\mathrm{n,p}}\cdot|\vec{F}_{\mathrm{n,p}}|}{v^{\mathrm{sat}}_{\mathrm{n,p}}}\right)^2}}, \tag{39}$$

Table 4: Parameter values for the mobility models.

Parameter	AlGaAs	InGaAs
μ_{n}^{0} [cm^2/Vs]	3000	6000
$v_{\mathrm{n}}^{\mathrm{sat}}$ [cm/s]	$1.2 \cdot 10^6$	$11.0 \cdot 10^6$
α_{n} [K^{-1}]	0.0431	0.0064
μ_{p}^{0} [cm^2/Vs]	120	120
$v_{\mathrm{p}}^{\mathrm{sat}}$ [cm/s]	$5.0 \cdot 10^6$	$5.0 \cdot 10^6$
α_{p} [K^{-1}]	$0.62 \cdot 10^{-3}$	$0.62 \cdot 10^{-3}$

where $\mu_{\mathrm{n,p}}^{0}$ are the zero-field mobilities, $v_{\mathrm{n,p}}^{\mathrm{sat}}$ are the saturation velocities, and $|\vec{F}_{\mathrm{n,p}}|$ are the magnitudes of the driving force for electrons and holes, respectively. The driving forces are governed by the equations

$$\vec{J}_{\mathrm{n}} = q \cdot n \cdot \mu_{\mathrm{n}} \cdot \vec{F}_{\mathrm{n}}, \quad \vec{J}_{\mathrm{p}} = q \cdot p \cdot \mu_{\mathrm{p}} \cdot \vec{F}_{\mathrm{p}}. \tag{40}$$

The HD mobility is modeled carrier temperature dependent

$$\mu_{\mathrm{n,p}}(T_{\mathrm{n,p}}) = \frac{\mu_{\mathrm{n,p}}^{0}}{1 + \alpha_{\mathrm{n,p}}(T_{\mathrm{n,p}} - T_{\mathrm{L}})}, \tag{41}$$

where $T_{\mathrm{n,p}}$ are the carrier temperatures and T_{L} is the lattice temperature. The corresponding values for the parameters can be found in Table 4.

4.7 Results

The device simulated in this study was fabricated using a structure grown by molecular beam epitaxy. From top to bottom the layer sequence consists of a highly doped GaAs cap layer, a $30\ \mathrm{nm}$ undoped $\mathrm{Al_{0.2}Ga_{0.8}As}$ barrier layer, a $12\,\mathrm{nm}$ $\mathrm{In_{0.2}Ga_{0.8}As}$ channel layer, and a $400\,\mathrm{nm}$ $\mathrm{Al_{0.2}Ga_{0.8}As}$ lower barrier layer on a semi-insulating GaAs-substrate. Within the upper barrier layer, a delta doping with an active

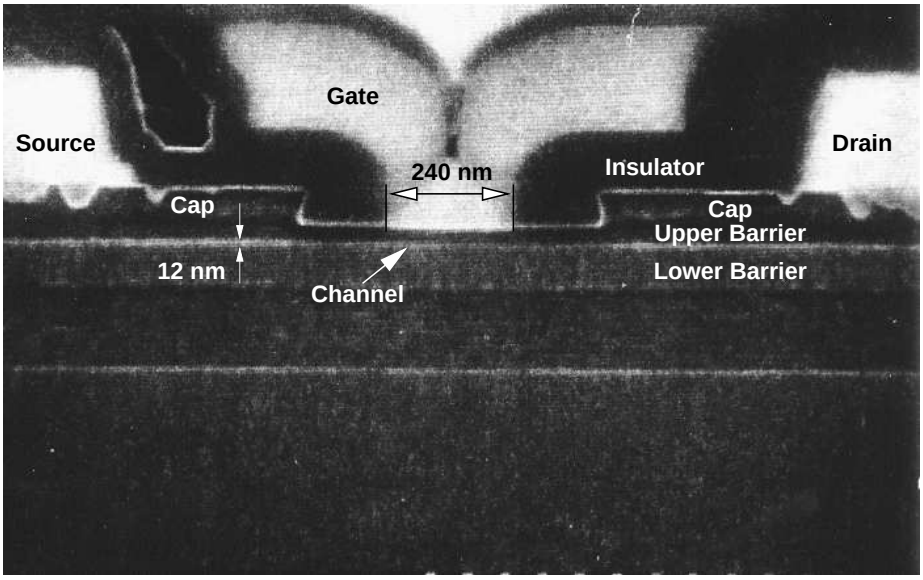

Figure 17: Representative scanning electron microscopy cross section of the HEMT.

doping concentration of about $N_D = 2.7 \cdot 10^{12}\ \mathrm{cm}^{-2}$ is grown. The $\mathrm{Al_{0.2}Ga_{0.8}As}$ barrier below the

channel contains a 7 nm thick doping layer with an active doping concentration of about $N_D = 8.5 \cdot 10^{11}\ \mathrm{cm}^{-2}$.

The gate length of the HEMT is $240\,\mathrm{nm}$. In the vicinity of the gate, the cap layer is etched to form a recess of about $540\mathrm{nm}$ length. The gate is placed symmetrically within the recess. Thus, ungated channel regions extend for about $150\ \mathrm{nm}$ at both sides of the gate. Fig. 17 shows a representative SEM-profile (Scanning

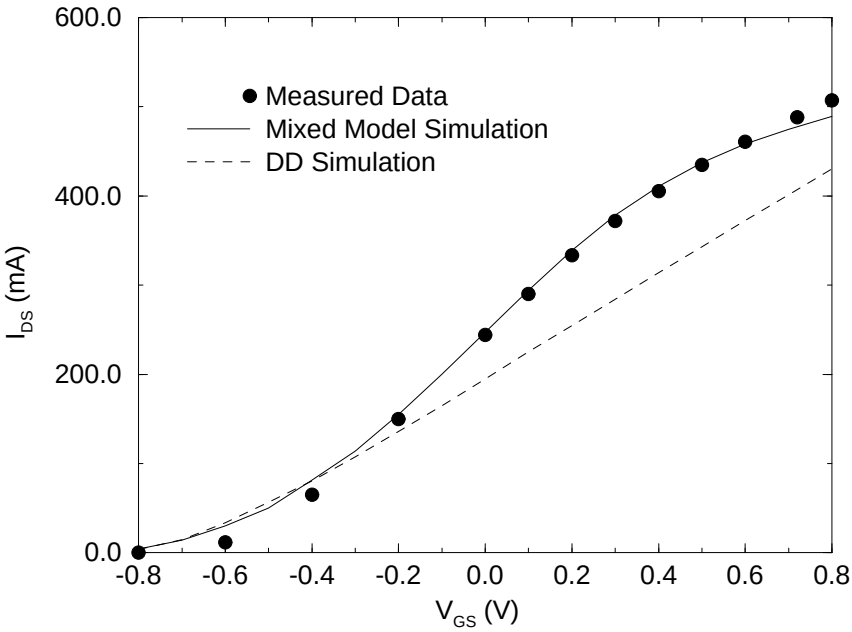

Figure 18: I-V curves for $\mathrm{V_{DS}} = 2\ \mathrm{V}$.

Electron Microscopy) of the structure. As can be seen, the alloying process of the ohmic contacts does not lead to complete penetration of the cap. Thus, we assume that the underlying heterostructures are not destroyed by the contacts. Therefore, the schematic structure shown in Fig. 16 where the ohmic metal is placed on top of the cap layer is used for simulation. For the two-dimensional simulations a contact resistance of $0.1\,\Omega\mathrm{mm}$ is assumed. The width of the device is $180\,\mu\mathrm{m}$ which results in a contact resistance of $0.6\ \Omega$ for the complete extrinsic device.

The mixed model simulation is performed with a hydrodynamic model within the channel region and a drift-diffusion model within the other layers. The hydrodynamic model is only applied to electrons. The hole concentration does not influence the device characteristics and the carrier temperature is taken into account implicitly by the dependence of the hole mobility on the driving force, i.e., the plain DD model is used for holes. A rectangular grid with 2726 points is used for discretization. The channel layer is discretized with 315 points. Thus, the mixed DD/HD model simulation needs about 1.2 times the computation time of a plain DD simulation and at least 0.7 times the computation time of a full HD simulation.

The simulation of one bias point requires an average of 500 iteration steps, 30 MB main memory, and needs 200 sec. CPU-time on an HP 9000/735 with 100 MHz clock frequency.

The measured transfer characteristic for a drain-source voltage of 2 V is shown in Fig. 18 along with two simulated I-V curves, one with plain DD model simulation the other with mixed model simulation. The measurement was performed on wafer on a $4 \times 45\ \mu\mathrm{m}$ device. As depicted in this figure the mixed model simulation and the measured data agree very well.

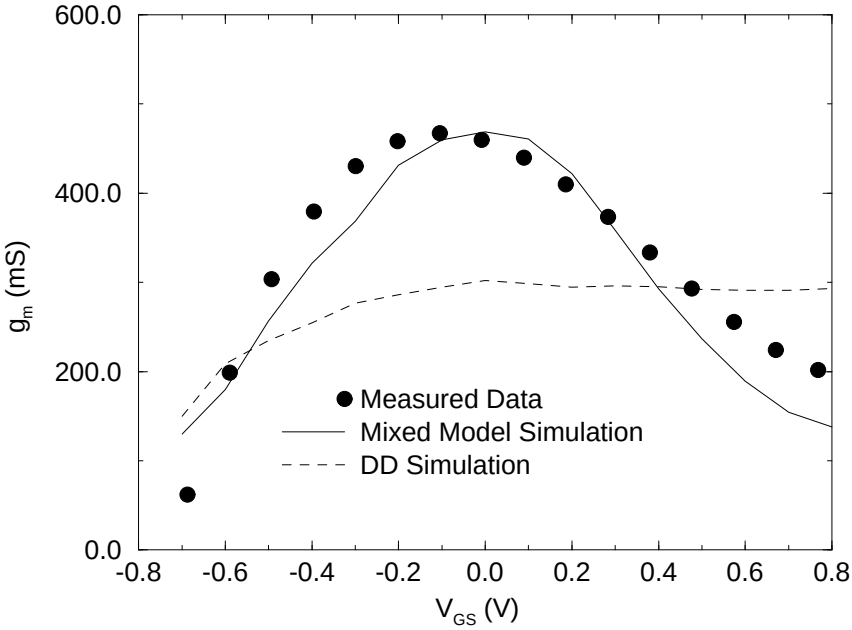

Figure 19: Transconductance for $V_{DS} = 2$ V.

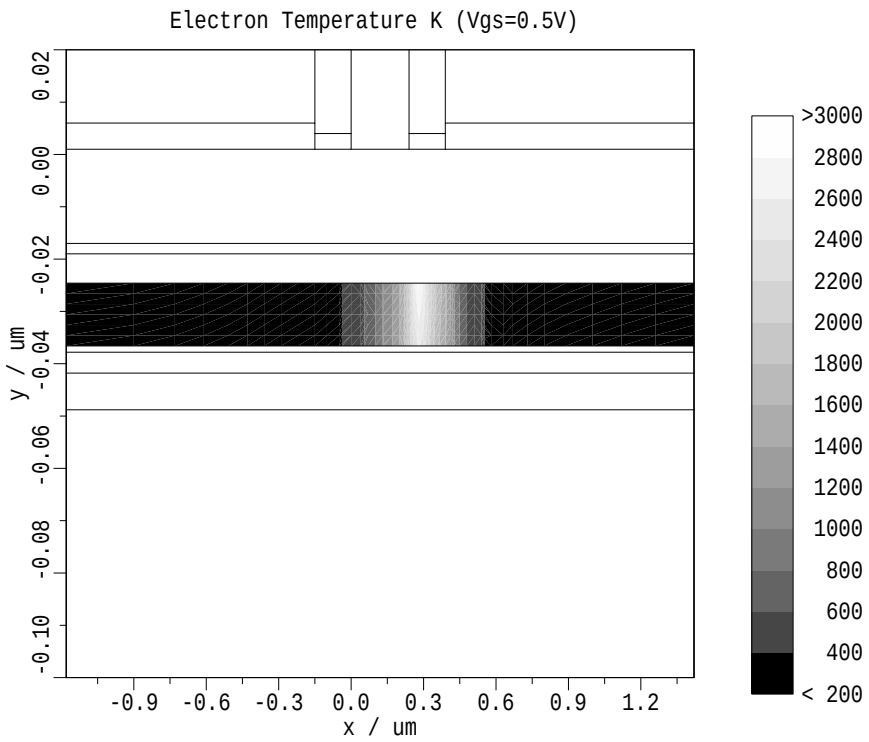

Figure 20: Electron temperature inside the channel layer ($V_{DS} = 2$ V, $V_{GS} = +0.5$ V).

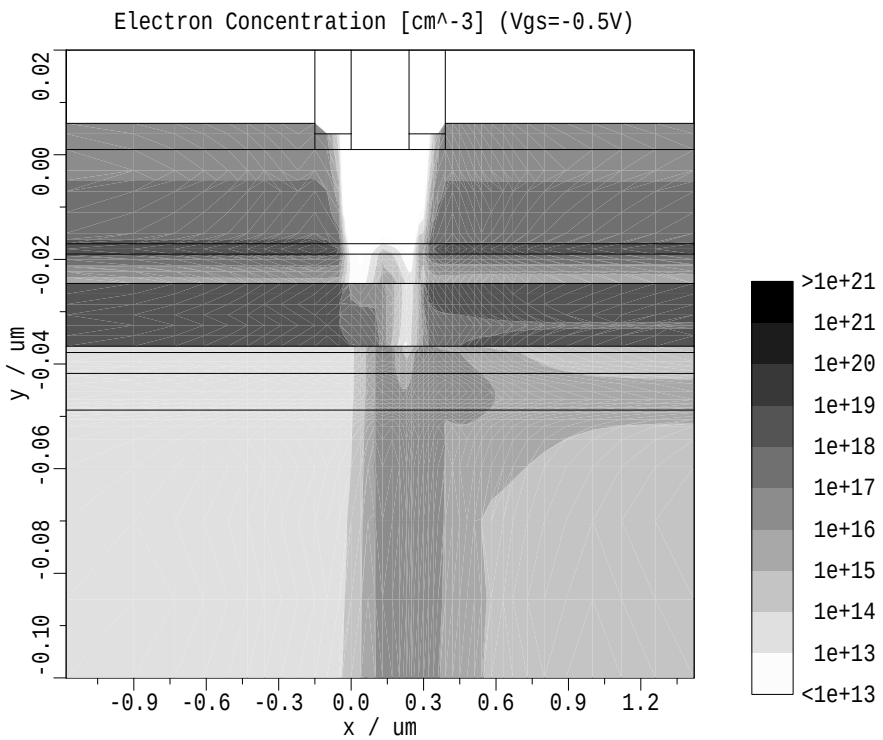

Figure 21: Electron concentration ($V_{DS} = 2$ V, $V_{GS} = -0.5$ V).

The transfer characteristics can be divided up into 3 operation regimes, each regime owing to a major physical effect. Firstly, the pinch off regime, i.e., negative gate voltages where the electron concentration in the channel is low but is starting to rise with the gate voltage increasing. Most of the current flowing is conducted in the lower barrier layer.

The deviation of the DD simulation and the measurement can be attributed to an overestimation of the electron confinement in the channel, i.e., the electrons are not swapped out into the lower barrier where their mobility is rather low. This is simulated much more realistically by the mixed model simulation as shown in Fig. 21.

The second regime is the one of most interest for device applications. The drain current is controlled mostly linear by the gate voltage and exhibits the maximum in g_m, as shown in Fig. 19.

For gate voltages higher than 0.3 V, marking the third regime, the I-V curve in Fig. 18 drops off since the electrons heat up and start to surmount the energy barrier between channel and the barrier layer above known as real-space transfer of the electrons. Hence, an increasing fraction of the electron transport takes place within the upper barrier layer where the electron mobility is much lower than within the channel. Fig. 20 shows the electron temperature inside the channel of the transistor and Fig. 22 the electron concentration of the entire device. As clearly can be seen in Fig. 20 the temperature is about 3000 K on the drain-sided end of the channel which allows the electrons easily to cross the heterojunction between channel and upper barrier layer.

Tunneling of electrons through the heterojunctions is important for the connection of the drain-sided end of the channel to the drain contact. When tunneling is not taken into account only few electrons are able to leave the channel and to reach the drain contact. Thus, the current is too low (see Fig. 18).

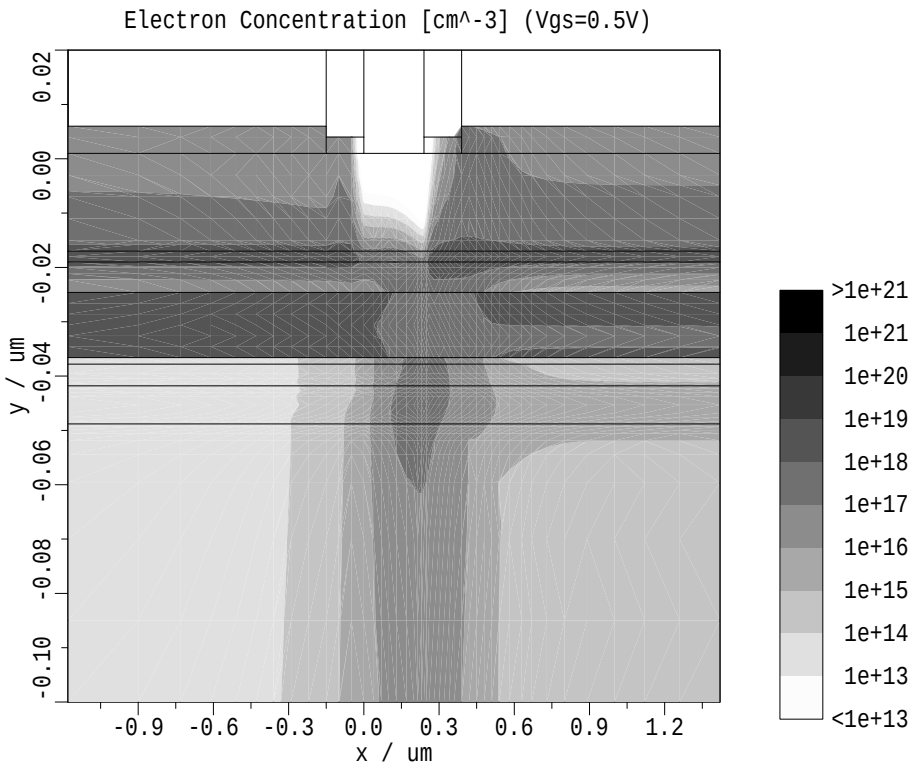

Figure 22: Electron concentration ($V_{DS} = 2$ V, $V_{GS} = +0.5$ V).

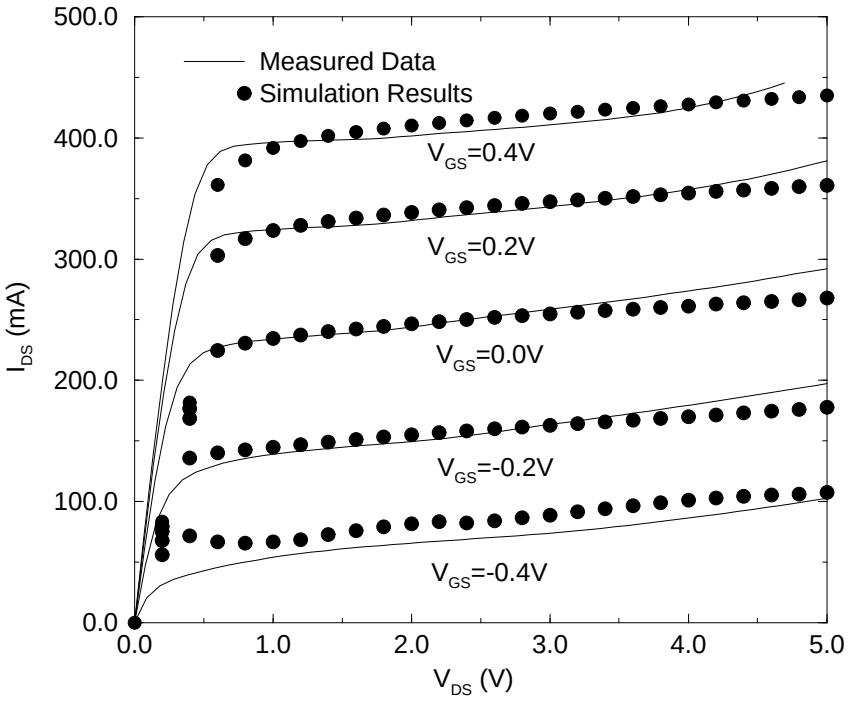

Figure 23: Output characteristics of the HEMT. The simulation results are in good agreement with the measured data.

In Fig. 23 the output characteristics of the HEMT are depicted. The simulation results are in good agreement with the measured data. The correspondence of the output conductance shows, that, as stated above, the current flow inside the channel and the neighboring segments is well characterized by the mixed model simulations.

4.8 Conclusion

A quarter micron delta-doped pseudomorphic double-heterojunction high electron mobility transistor is simulated with the generic two-dimensional device simulator MINIMOS-NT. A new method is used which divides the device region into several subdomains, referred to as segments, each segment with its specific physical models. This offers the opportunity to combine segments where a hydrodynamic model is used with segments where the plain drift-diffusion model is employed. Thus, for the channel of the transistor, where short channel effects are expected, the energy balance equations are used to account for non-local effects such as velocity overshoot. Furthermore, solving the hydrodynamic model in only a part of the device is more efficient than a full hydrodynamic solution.

Moreover, the distinct segments are linked together with specific interface models. These interface models allow to deal with abrupt heterojunctions and to include the effects of thermionic-field emission which determine the current confinement within the channel layer and properly describe how the carriers swap out into the neighboring segments. Hence, the reduction of the transconductance by real-space transfer can be observed by the simulations.

The combination of abrupt heterojunctions and a two-dimensional mixed hydrodynamic drift-diffusion model simulation leads to reasonable results which are in good agreement with the measured data. Furthermore, the influence of several physical effects, such as real-space transfer and carrier heating, on the device characteristics can be identified.

References

[1] W. Tuppa and S. Selberherr. A CASE-Oriented Configuration Management Utility. In M.H. Hamza, editor, *Proc. IASTED/ISMM Int. Conf. on Modelling and Simulation*, pp 83–87, Pittburgh, Pennsylvania, USA, 1996.

[2] F. Fasching. *The Viennese Integrated System for Technology CAD Applications–Data Level Design and Implementation*. Dissertation, Technische Universität Wien, 1994.

[3] H. Puchner. *Advanced Process Modeling for VLSI Technology*. Dissertation, Technische Universität Wien, 1996.

[4] A.R. Alvarez, editor. *BiCMOS Technology and Applications*. Kluwer, second edition, 1993.

[5] Ch. Pichler and S. Selberherr. Rapid Semiconductor Process Design within the VISTA Framework: Integration of Simulation Tools. In M.H. Hamza, editor, *Proceedings of the IASTED International Conference*, Modelling and Simulation, pp 147–150, Pittsburgh, PA, USA, 1993. The International Association of Science and Technology for Development.

[6] E. Strasser and S. Selberherr. Algorithms and Models for Cellular Based Topography Simulation. *IEEE Trans.Computer-Aided Design*, 14(9):1104–1114, 1995.

[7] W.G. Oldham, A.R. Neureuther, C. Sung, J.L. Reynolds, and S.N. Nandgaonkar. A General Simulator for VLSI Lithography and Etching Processes: Part II — Application to Deposition and Etching. *IEEE Trans. Electron Dev.*, 27(8):717–722, 1980.

[8] W.G. Oldham, A.R. Neureuther, C. Sung, J.L. Reynolds, and S.N. Nandgaonkar. A General Simulator for VLSI Lithography and Etching Processes: Part II–Application to Deposition and Etching. *IEEE Trans.Electron Devices*, ED-27(8):1455–1459, 1980.

[9] A. Forghieri, R. Guerrieri, P. Ciampolini, A. Gnudi, M. Rudan, and G. Baccarani. A New Discretization Strategy of the Semiconductor Equations Comprising Momentum and Energy Balance. *IEEE Trans.Computer-Aided Design*, 7(2):231–242, 1988.

[10] T.W. Tang. Extension of the Scharfetter-Gummel Algorithm to the Energy Balance Equation. *IEEE Trans.Electron Devices*, ED-31(12):1912–1914, 1984.

[11] W.-S. Choi, J.-G. Ahn, Y.-J. Park, H.-S. Min, and C.-G. Hwang. A Time Dependent Hydrodynamic Device Simulator SNU-2D With New Discretization Scheme and Algorithm. *IEEE Trans.Computer-Aided Design*, 13(7):899–908, 1994.

[12] T.-W. Tang and M.-K. Ieong. Discretization of Flux Densities in Device Simulations Using Optimum Artificial Diffusivity. *IEEE Trans.Computer-Aided Design*, 14(11):1309–1315, 1995.

[13] T. Simlinger, H. Kosina, M. Rottinger, and S. Selberherr. MINIMOS-NT: A Generic Simulator for Complex Semiconductor Devices. In H.C. de Graaff and H. van Kranenburg, editors, *ESSDERC'95 - 25th European Solid State Device Research Conference*, pp 83–86, Gif-sur-Yvette Cedex, France, 1995. Editions Frontieres.

[14] R. Vankemmel, W. Schoenmaker, R. Cartuyvels, and K. De Meyer. Implementation of Heterojunctions into the 2-D Finite-Element Simulator Prism: Some Scaling Considerations. *Solid-State Electron.*, 35(4):571–578, 1992.

[15] J.Y.F. Tang and S.E. Laux. MONTE: A Program to Simulate the Heterojunction Devices in Two Dimensions. *IEEE Trans.Computer-Aided Design*, CAD-5(4):645–652, 1986.

[16] K. Yang, J.R. East, and G.I. Haddad. Numerical Modeling of Abrupt Heterojunctions Using a Thermionic-Field Emission Boundary Condition. *Solid-State Electron.*, 36(3):321–330, 1993.

[17] J.R. Jones, G.B. Tait, S.H. Jones, and D.S. Katzer. DC and Large-Signal Time-Dependent Electron Transport in Heterostructure Devices: An Investigation of the Heterostructure Barrier Varactor. *IEEE Trans.Electron Devices*, 42(8):1393–1403, 1995.

[18] D. Schröder. *Modelling of Interface Carrier Transport for Device Simulation*. Springer, 1994.

[19] R.E. Bank and D.J. Rose. Parameter Selection for Newton-like Methods Applicable to Nonlinear Partial Differential Equations. *SIAM J.Numer.Anal.*, 17(6):806–822, 1980.

[20] R.E. Bank and D.J. Rose. Global Approximate Newton Methods. *Numer.Math.*, 37:279–295, 1981.

[21] H.A. van der Vorst. BI-CGSTAB: A Fast and Smoothly Converging Variant of BI-CG for the Solution of Nonsymmetric Linear Systems. *SIAM J.Sci.Stat.Comput.*, 13(2):631–644, 1992.

[22] C. Fischer and S. Selberherr. Optimum Scaling of Non-Symmetric Jacobian Matrices for Threshold Pivoting Preconditioners. In *Int. Workshop on Numerical Modeling of Processes and Devices for Integrated Circuits NUPAD V*, pp 123–126, Honolulu, 1994.

[23] Y. Saad. Preconditioning Techniques for Nonsymmetric and Indefinite Linear Systems. *J.Comp.Appl.Math.*, 24:89–105, 1988.

[24] P. Bhattacharya, editor. *Properties of Lattice-Matched and Strained Indium Gallium Arsenide*. Number 8 in EMIS Datareviews Series. IEE INSPEC, 1993.